

Bullseye Analysis: A Fluorescence Microscopy Technique to Detect Local Changes in Intracellular Reactive Oxygen Species (ROS) Production

Joshua G Hughes, David R Chisholm, Andrew Whiting, John M Girkin, Carrie A Ambler



Bullseye Analysis: A Fluorescence Microscopy Technique to Detect Local Changes in Intracellular Reactive Oxygen Species (ROS) Production

Joshua G. Hughes^{1,2} , David R. Chisholm^{2,3}, Andrew Whiting^{2,3}, John M. Girkin^{4,*} and Carrie A. Ambler^{1,2,*} 

¹Department of Biosciences, Durham University, Durham DH1 3LE, UK

²LightOx Limited, 65 Westgate Road, Newcastle-Upon-Tyne NE1 1SG, UK

³Department of Chemistry, Durham University, Durham DH1 3LE, UK

⁴Department of Physics, Durham University, South Road, Durham DH1 3LE, UK

*Corresponding author: John M. Girkin, E-mail: j.m.girkin@durham.ac.uk; Carrie A. Ambler, E-mail: c.a.ambler@durham.ac.uk

Abstract

Reactive oxygen species (ROS) are naturally produced compounds that play important roles in cell signaling, gene regulation, and biological defense, including involvement in the oxidative burst that is central to the anti-microbial actions of macrophages. However, these highly reactive, short-lived radical species also stimulate cells to undergo programmed cell death at high concentrations, as well as causing detrimental effects such as oxidation of macromolecules at more moderate levels. Imaging ROS is highly challenging, with many researchers working on the challenge over the past 10–15 years without producing a definitive method. We report a new fluorescence microscopy-based technique, Bullseye Analysis. This methodology is based on concepts provided by the FRAP (Fluorescence Recovery after Photobleaching) technique and refined to evidence the spatiotemporal production of ROS, and the subsequent consequences, on a subcellular scale. To exemplify the technique, we have used the ROS-reporter dye, CellROX, and the ROS-inducing photosensitizer, LightOx58, a potent source of ROS compared with UV irradiation alone. Further validation of the technique was carried out using differing co-stains, notably Mitotracker and JC-1.

Key words: bullseye analysis, microscopy, photodynamic therapy (PDT), photosensitizer, phototoxicity, reactive oxygen species (ROS)

Introduction

Reactive oxygen species (ROS), such as hydrogen peroxide and superoxide, are members of a family of highly reactive molecules that cause oxidative modifications of biomacromolecules. Within cells, ROS production often causes oxidative stress-induced pathology by damaging lipids, proteins, and DNA (Cross et al., 1987; Nespolo, 2017; Sies, 2019). However, in the past two decades, it has become apparent that ROS also act as signaling molecules that regulate numerous biological and physiological processes (Finkel, 1998; Sies, 2019). One of the best characterized sources of ROS are mitochondria, which produce the superoxide radical ($O_2^{\bullet-}$) when oxygen is prematurely and incompletely reduced during respiration. In addition to natural sources of ROS, the irradiation of fluorescent molecules in the presence of molecular oxygen can lead to ROS formation by one of two proposed processes: (i) through a photo-induced electron transfer (redox reaction) mainly producing $O_2^{\bullet-}$ and HO_2^* (type-I process), or (ii) through an energy transfer to produce single oxygen (1O_2) (type-II process; Baptista et al., 2017). The ability to induce ROS-mediated, light-activated cytotoxic processes from the excitation of a fluorescent photosensitizer has been harnessed as a powerful, non-surgical therapeutic technique for the eradication of a range of epithelial cancers (Baptista et al., 2017; Zhang et al., 2018a; de Albuquerque et al., 2019).

Studying the spatiotemporal distribution of intracellular ROS with high resolution, specificity, and sensitivity has been important in dissecting some of the complexities of ROS production and signaling. The main ROS detection methods within biological systems are indirect reporters: fluorescence (synthetic and genetically encoded), chemi-luminescence, and spectro-photometric; while direct measurement is achievable through highly complex methods including electron paramagnetic resonance (EPR) and electron spin resonance (ESR); however, these are not biologically compatible (Wang et al., 2013; Zhang et al., 2018b; Fuloria et al., 2021). For indirect reporters, species/organelle specificity and linearity of detection must be considered carefully for reliable measurement and analysis. Focusing on spatial and temporal resolution, significant progress has been made in ROS imaging at the level of intact cells, with the development of novel fluorescent synthetic ROS indicators that are species- and organelle-specific. The development of such indicator dyes has occurred in parallel with significant advancements in microscopy techniques. Specifically, the development of improved high speed, sensitive detectors for both point scanning and wide-field imaging systems (Girkin, 2019). Furthermore, two-photon excitation has enabled precise excitation and measurement of ROS-reporters while minimizing artificial ROS production from short wavelength excitation (Wang et al., 2017; Murfin et al., 2019).

Received: September 18, 2022. Revised: October 28, 2022. Accepted: November 6, 2022

© The Author(s) 2022. Published by Oxford University Press on behalf of the Microscopy Society of America.

This is an Open Access article distributed under the terms of the Creative Commons Attribution License (<https://creativecommons.org/licenses/by/4.0/>), which permits unrestricted reuse, distribution, and reproduction in any medium, provided the original work is properly cited.

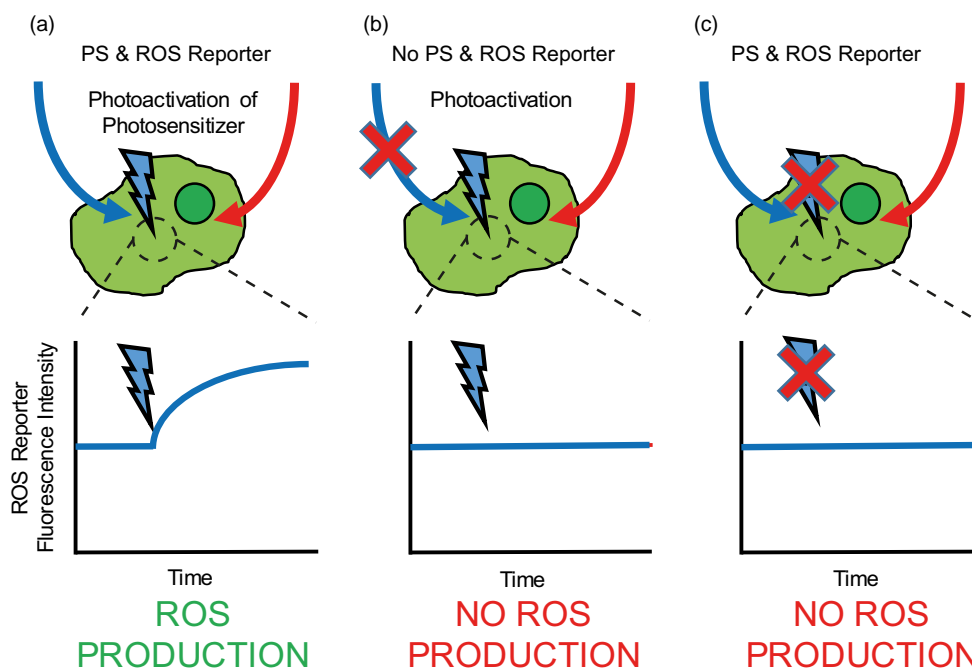


Fig. 1. Principles of activation method. ROS reporter fluorescence intensity versus time, following localized photoactivation of a ROS producing molecule (photosensitizer). In the presence of a photosensitizer (PS) and a ROS reporter, localized photoactivation of the photosensitizer will produce ROS and increase the fluorescence intensity of the reporter with respect to the rest of the cell (a). Without a photosensitizer in the system (b), or photoactivation (c), there will be no ROS production.

Here, we report a significant advance in measuring and quantifying localized, subcellular ROS production in a spatial and time-dependent manner. The concept is based upon the widely used Fluorescence Recovery after Photobleaching (FRAP) approach but with a new approach to the data analysis to provide information on local ROS changes. By using a fluorescent ROS reporter, accurate ROS production can be measured in both space and time, within and immediately surrounding, the area of ROS production. The principles of this approach are depicted in Figure 1, in which a photosensitizer is used to generate localized ROS, purely to exemplify the approach. The concentration of ROS within a photoactivated (irradiation of a ROS-generating photosensitizer) region will increase and, therefore, the fluorescence intensity of a ROS-reporting fluorophore should increase concomitantly. As controls, the absence of localized photoactivation, or the ROS-generating photosensitizer, should result in no increase in ROS. Further analysis has been achieved by measuring the fluorescence as a function of both time and of distance (radius) from the center of the region of interest (ROI), which we have termed “Bullseye Analysis”. This facilitates analysis of the diffusion front between the area of ROS production and the immediate surrounding area, and its time evolution. To exemplify this experimentally, we have used a ROS-generating (photosensitizing) fluorescent dye LightOx58, previously demonstrated to have localized cell distribution (de Pablo et al., 2018; Chisholm et al., 2019; *in cellulo* excitation/emission = 405/510 nm; de Pablo et al., 2018, 2020) and the ROS-reporter, CellROX (Ex/Em = 633/665 nm).

Methods

Cell Culture

HaCaT human epidermal keratinocytes were purchased from a commercial supplier (Thermo Fisher) and the cell line was cultured at 37°C/5% CO₂ in DMEM (Gibco Cat. No.

10566, high glucose, GlutaMAX supplement) with 10% fetal bovine serum (ThermoFisher, Cat. No. 10270-106) and 1% penicillin/streptomycin (ThermoFisher, Cat. No. 15070-063).

Cell Plating

Ibidi μ -Slide 8 Well Glass Bottom plates (Thistle Scientific, Cat. No. 80827-90) were used for imaging. 200 μ L of a 200,000 cells/mL solution was added to each well, to be stained and imaged the following day.

Cell Labeling

LightOx58 was acquired from LightOx Ltd. (de Pablo et al., 2018, 2020; Chisholm et al., 2019). Working solutions were diluted from 1 mM stock solutions dissolved using dimethyl sulfoxide. Staining solutions were comprised of pre-heated media with 1 μ M LightOx58, 5 μ M CellROX Deep Red (ThermoFisher, Cat. No. C10422), 200 nM MitoTracker® Red CMXRos (ThermoFisher, Cat. No. M7512), and 2.5 μ g/mL JC-1 (ThermoFisher, Cat. No. M34152), dependent on the sample. The cells were incubated with the labeling solutions for 30 min at 37°C before being washed with phosphate-buffered saline (ThermoFisher, Cat. No. 20012019). Live Cell Imaging Solution (ThermoFisher, Cat. No. A14291DJ) was added to each well for imaging purposes.

Imaging

A Leica Sp5 Laser Scanning confocal microscope was used to conduct the FRAP experiments on LightOx58 (Supplementary Fig. S1) to assess its motility. Cells were imaged in an environmentally controlled chamber, at 37°C. A HCX PL APO lambda blue 63.0 \times /1.40 OIL UV objective lens was utilized for these experiments.

A Zeiss 880 Laser Scanning Confocal microscope was used for the remainder of the work. Cells were imaged in an environmentally controlled chamber, at 37°C, 5% CO₂. A Plan-Apochromat 63×/1.4 Oil DIC M27 objective lens was utilized for these experiments. Images were obtained using Zen Black software (Zeiss), where the *time series*, *bleaching*, and *regions* software features were used to conduct the experiments. For the CellROX experiments, the pinhole was opened from the recommended setting of 1 Airy unit to 8 Airy units. This was to maximize the light collection and information obtained from a thicker optical section, while minimizing the excitation power required to reduce perturbation of the cells.

For imaging settings, see the [Supplementary Information](#).

Analysis

The analysis was similar to standard FRAP experiments (Kang et al., 2012). Pixel intensity data for the cells and regions of interest were extracted from the microscopy images by custom-written macros in the image analysis software *ImageJ* (Schindelin et al., 2012; Schneider et al., 2012). Pixel intensity values at each time point were taken for each ROI, as well as the entirety of the fluorescent regions of the cells within the microscopy images, which were used to correct for fading during imaging in the subsequent analysis. To select the fluorescent regions, thresholding and particle analysis was utilized. This data was subsequently analyzed using custom software written in *Python* 3.7. FRAP data were corrected for background and image fading via the equation (Kang et al., 2012):

$$F_{\text{corrected}}(t) = \frac{f(t) - f_{\text{bk}}(t)}{f_{\text{fade}}(t) - f_{\text{bk}}(t)}, \quad (1)$$

where $f(t)$ is the raw pixel intensity within the ROIs, $f_{\text{bk}}(t)$ is the background intensity levels, and $f_{\text{fade}}(t)$ is the intensity of the cells, minus the ROIs. This is used to correct for fading during imaging. The equation is then normalized to unity via,

$$F(t) = \frac{F_{\text{corrected}}(t)}{F_{\text{corrected}}^i}, \quad (2)$$

where $F_{\text{corrected}}^i$ is the averaged intensity of the corrected pre-bleaching frames. The first data point was not included in the normalization, as the intensity was significantly lower than the subsequent data points. LightOx58 FRAP (Supplementary Fig. S1) curves were fitted to linear, mono-exponential, and bi-exponential curves via χ^2 minimization. The curves of best fit were chosen via the R^2 statistic.

Mobile fraction, M_f , was calculated via:

$$M_f = \frac{F_{\infty} - F_0}{F_i - F_0}, \quad (3)$$

where F_{∞} is the long-term, steady-state value for fluorescence intensity post-bleach calculated from the equations of best fit and F_0 is the fluorescence intensity immediately after bleaching.

A two-sided Kolmogorov–Smirnov test was calculated using *scipy.stats.kstest* module within *Python*.

Bullseye Analysis

“Bullseye Analysis” measured the fluorescence intensity as both a function of time and of radius from the center of a circular ROI. A custom written *ImageJ* macro measured the intensity as a function of time for circular regions varying between

1-pixel radius and four times the bleaching ROI radius, for each ROI. The data were subsequently analyzed in a *Python* script, in which normalization corrections were performed using Equation (2). A moving average of 6 was used to smooth the data. The *Python* module *scipy curve_fit* was used to calculate the parameters of Equation (4) for each time point, while *sklearn LinearRegression* was used to calculate the gradient of ω^2 against t . The green channel data for JC-1 was normalized to the first time point post-photoactivation to correct for photo-bleaching during irradiation.

Results

Localized ROS quantification

To exemplify localized ROS production experimentally, a source of localized ROS and a ROS indicator were required. To this end, the photosensitizer LightOx58 and a spectrally distinct ROS reporter, CellROX, were used in conjunction within HaCaT cells. LightOx58 possesses a highly lipophilic structure that enables rapid entry into mammalian cells and has been shown to localize primarily at organelle membranes and lipid droplets (de Pablo et al., 2018; Chisholm et al., 2019, 2020). Activation at 405 nm elicits the local generation of ROS in cells, oxidizing CellROX and, thus, enabling local detection of ROS at Ex/Em = 633/665 nm. A standard FRAP characterization of LightOx58 was first conducted using a Leica Sp5 (see Supplementary Fig. S1) in order to measure the motility of the photosensitizer. A mobile fraction, M_f , of 0.66 was measured, while the 633 nm control confirmed the laser line did not activate the photosensitizer.

In the two-step process, the photosensitizer elicits the localized generation of ROS by being precisely photoactivated by a relevant laser line (405 nm) in a small region of the cell (5 μm diameter). Subsequently, in step two, the ROS level in this region is detected by the fluorescent ROS indicator. At each time point, the ROS levels are measured across the whole cell and are used to normalize the measured ROS levels within the localized regions of photosensitizer photoactivation. Therefore, any detected increase in ROS above these baseline measurements reflects a true localized effect, and not a consequence of whole-cell stress. To ascertain a dose-response relationship between localized photoactivation, ROS generation and subsequent CellROX fluorescence, the level of localized photoactivation was varied; zero, low, medium, and high photoactivation corresponding to 0, 1, 10, and 50% laser power, respectively (see Fig. 2). In the cases where the photosensitizer was present and photoactivated (Figs. 2b–2d), significant increases in localized ROS levels were detected. The measured ROS levels increase with photoactivation up to “medium,” indicating some form of dose-response relationship, however there is no significant difference between medium and high. In the absence of photoactivation (Fig. 2a), or the absence of an ROS source (Figs. 2f–2h), the ROS levels did not change significantly. A slight increase in Figure 2h can be attributed to phototoxicity at that level of irradiation.

Bullseye

To further explore how localized ROS production varies and develops in and around the photoactivated region of interest, our Bullseye Analysis was employed. The technique measures ROS-reporter intensity as a function of both time and radius from the center of the localized photoactivation region by

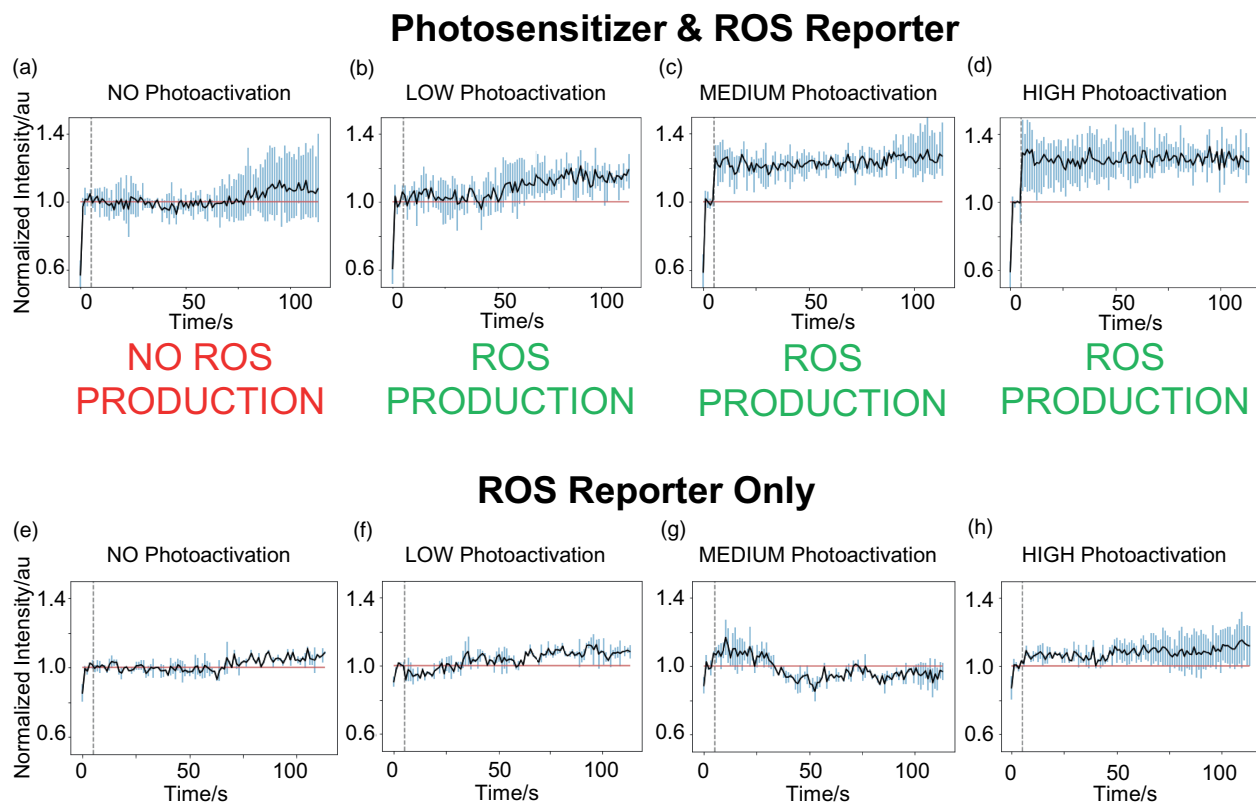


Fig. 2. Normalized fluorescence intensity of the ROS reporter (CellROX) as a function of time following localized photoactivation of a photosensitizer (LightOx58) with HaCaT cells. (a–d) Photosensitizer present, (e–h) no photosensitizer present. Photoactivation levels are 0, 1, 10, and 50% (left to right) of the maximum output of a 405 nm laser line for 5 imaging frames, indicating by the vertical dashed lines. The horizontal lines correspond to the initial pre-bleach fluorescent intensity levels and are included as a visual guide. The error bars are the range ($n=3$). The statistics and p -values from the Kolmogorov–Smirnov test for no, low, medium, and high photoactivation are 0.22 and 1.56×10^{-2} , 0.55 and 3.04×10^{-14} , 0.95 and 5.60×10^{-50} and 0.95 and 5.60×10^{-50} , respectively.

measuring, and averaging, rings of intensity (Fig. 3e). The spatial data can therefore be reduced to radius alone, which eases interpretation and modeling. However, one must be careful when considering spatial symmetry about the ROI. While the data are normalized at all spatial positions, the nucleus and cell membrane may impair data. Hence, effort was placed on the size and position of ROIs, situating them in central regions of the cytoplasm. Using the technique to analyze the data from the previous figure, we can see that a diffusion profile is visible immediately after photoactivation for “Medium” and “High” levels. ROS concentration levels are elevated above initial levels within and immediately around the photoactivation region, plateauing off to baseline levels with distance. There is no quantifiable difference between “No” and “Low” levels of photoactivation, reflecting the results in Figure 2.

To study the diffusion from the photoactivation region, we employed a similar analysis method to that previously employed in FRAP experimentation reported by Seiffert & Oppermann (2005). This uses the analytical solution to the diffusion equation (Fick’s second law):

$$I(x, t) = I_0 + A(t) \cdot \exp\left(-\frac{x^2}{2\omega^2}\right), \quad (4)$$

where I is the fluorescence intensity at position x and time t post-photoactivation, I_0 is the pre-photoactivation fluorescence intensity, ω is the Gaussian width, and D is the diffusion coefficient. $A(t)$, in the case of FRAP, is the depth of the “dip”

in intensity post-bleaching; however, in our case, this will be the increase in fluorescence intensity due to ROS generation within the ROI and thus the sign is reversed. By plotting the square of the Gaussian width, ω^2 , against time, t , the diffusion coefficient will correspond to the gradient.

We can see that the Gaussian width increases with time (Figs. 3g, 3h) as the fluorescence of CellROX diffuses outwards from the photoactivation spot leading to a diffusion coefficient of $1.6 \pm 0.2 \mu\text{m}^2/\text{s}$.

Impact of Cell Stress

To test the reproducibility of our approach and the dose-response relationship, further technical repeats (datasets) (Fig. 4, Datasets B and C) were produced. The datasets were broadly similar across all photoactivation levels, but for one exception: at the highest level of photoactivation, a significant difference was observed between datasets. Instead of the measured ROS levels increasing rapidly and remaining stable as noticed in Dataset A, Datasets B and C rapidly increased followed by a steady decline well below the pre-photoactivation step. This striking variation in CellROX dye response at high photoactivation was unexpected and we hypothesized that biological variation in the basal levels of ROS evident prior to the experiment may contribute to the observed variation. To examine this, further datasets were acquired, and ROS reporter intensity levels before the experiment were measured (Figs. 4m–4p). Datasets that had exhibited relatively low

Photosensitizer & ROS Reporter

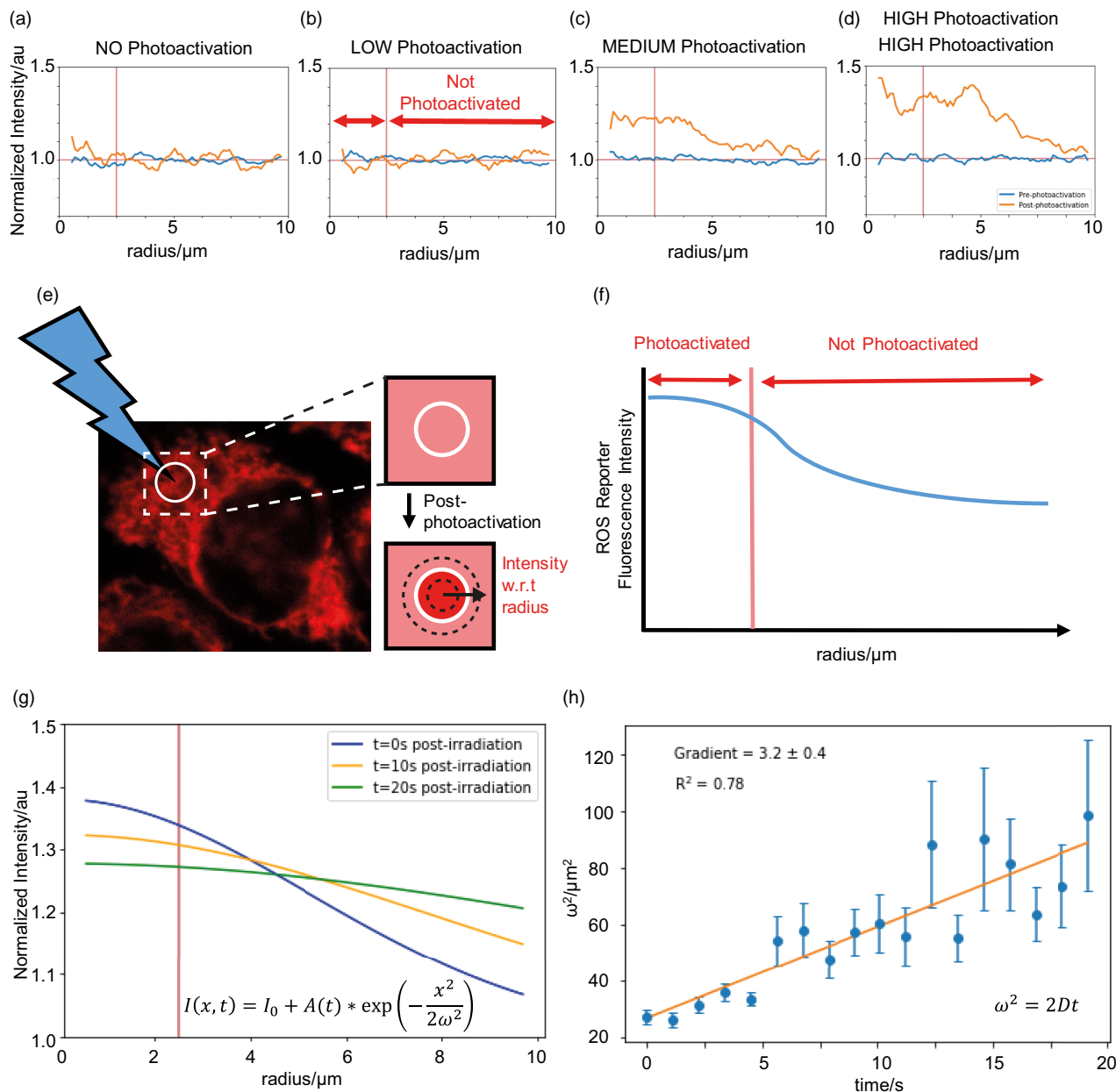


Fig. 3. Bullseye Analysis. ROS reporter (CellROX) normalized fluorescence intensity as a function of radius from the center of the photoactivated region and of time following localized photoactivation of the photosensitizer. **(a–d)** Photoactivation levels are 0, 1, 10, and 50% of the maximum output of a 405 nm laser line. The horizontal line corresponds to the averaged initial fluorescent intensity and the vertical line corresponds to the radius of the photoactivated area are included as visual guides. The blue line is from the first pre-photoactivation frame, while the orange line is from the initial post-photoactivation frame, $n=3$. **(e)** A schematic of the Bullseye Analysis showing the pixel rings superimposed to measure the intensity produced as a function of radius. **(f)** The associated graph is hypothetical illustrating an example of the expected model result. **(g, h)** Experimental data as collected in the high activation model (panel **d**) was analyzed using the Bullseye method. **(g)** Fluorescence intensity curves for 3 time points (t =time) fitted to the data using the solution of Fick’s law [equation shown; Eq. (4)]. **(h)** Gaussian width (ω^2) of the diffusion curve (panel **g**) plotted against time. The gradient is calculated and plotted using linear regression and the associated standard error.

ROS reporter fluorescence intensities (0–20) had a higher increase in ROS levels post-photoactivation and were less likely to reduce over time. Those that had a higher (30+) initial intensity showed smaller increases, and had a higher likelihood of a significant decrease in ROS reporter intensity post-photoactivation. These results suggest that intrinsic cell stress and baseline ROS levels prior to the experiment could

influence the experimental outputs and, thus, are important measurements to collect.

Localized ROS Effect Upon Mitochondria

From the previous data, it was clear that we were obtaining unexpected results at higher levels of photoactivation and

Photosensitizer & ROS Reporter

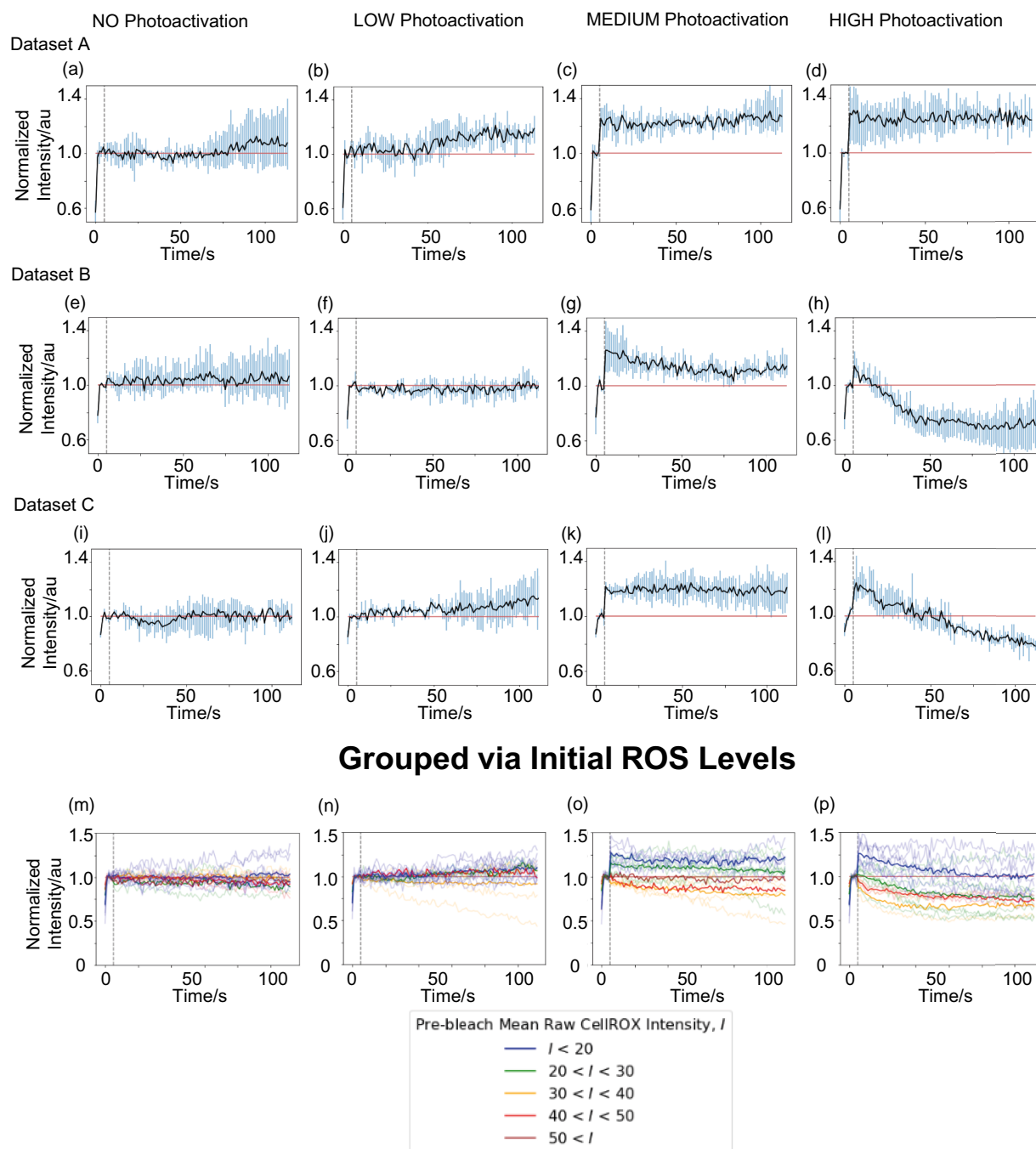


Fig. 4. ROS reporter fluorescence intensity post-photoactivation has dependency on the initial ROS levels. **(a–l)** Datasets A, B, and C show normalized fluorescence intensity of the ROS reporter in HaCaT cells as a function of time following localized photoactivation of photosensitizer at various photoactivation levels. The error bars are the range ($n=3$). **(m–p)** Data grouped by initial ROS reporter levels. The individual datasets ($n=18$) are shown by translucent curves and the average for each group is overlaid.

thus ROS generation in our exemplification system. To further probe ROS generation in the system, and test the suitability of the technique with differing co-stains, MitoTracker and JC-1 were used in place of CellROX.

Mitochondria are a prime source of intracellular ROS for essential redox signaling (Holmström & Finkel, 2014); however, evidence suggests that localized ROS also leads to oxidative damage to mitochondrial proteins, membranes and DNA, impairing the ability of mitochondria to carry out their wide

range of metabolic functions (Ott et al., 2007). To better understand the effect of high localized ROS production upon mitochondria, the photoactivation experiment was repeated with the mitochondria-targeting fluorophore, MitoTracker Red CMXRos in place of CellROX.

Clear differences in cell morphology were evident when we compared the microscopy images of the MitoTracker with (Fig. 5a) and without (Fig. 5b) the photosensitizer and subsequent 405 nm photoactivation. In the MitoTracker-only

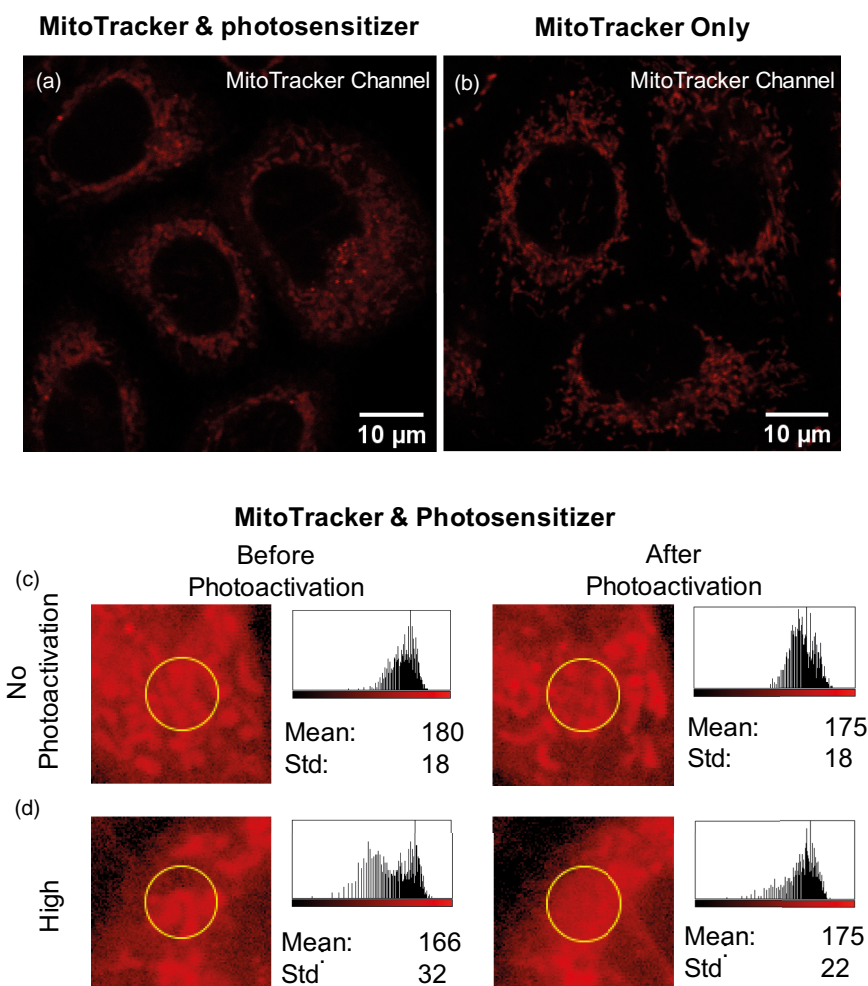


Fig. 5. Photosensitizer effects on mitochondria. Confocal microscopy image of mitochondria prior to photoactivation; (a) MitoTracker Red only and (b) MitoTracker Red and photosensitizer within HaCaT cells. (c) Linear and (d) logarithmic look-up tables of cell before and after high photoactivation when incubated with MitoTracker Red and LightOx58. Histograms on the regions within the circles are shown below. The circular ROI in panel d has been manually adjusted to correct for slight drift during imaging. The histogram of pixel intensity values included with the mean and standard deviation. The standard deviation changes from 32 prior to photoactivation, where mitochondria are bright with a dim background, to 22 post-photoactivation. (c) Conversely in the control mitochondria structure was retained post-activation and the standard deviation remained constant.

scenario, the mitochondria appeared more defined than in the cells incubated with the photosensitizer. As MitoTracker is dependent upon the mitochondrial membrane potential for accumulation (Poot et al., 1996), this suggested a reduction in the membrane potential, without depolarization, as the mitochondria structure remained visible. Therefore, although the photosensitizer has minimal dark toxicity, which is the toxicity of the photosensitizer without irradiation, its presence did elicit slight perturbation of the cell. ROIs in which “no” and “high” photoactivation was used are shown in Figures 5c and 5d with logarithmic look-up tables (LUTs). A logarithmic LUT was utilized to enhance differences over a wide dynamic range so that certain detail is more easily visualized than with standard linear LUTs. Within the ROI of the high activation scenario, mitochondria structure and definition visible prior to photoactivation is lost, suggesting depolarization has occurred and MitoTracker has leaked out into the cytoplasm.

To enable a more robust quantitative measure of the photosensitizer effects upon the mitochondrial membrane potential, the technique was repeated with JC-1 (Ex/Em = 488/530 monomeric, 590 nm aggregated), a mitochondrial membrane

potential indicator, in place of CellROX and MitoTracker (Fig. 6). When mitochondria are healthy, JC-1 is accumulated and aggregates in the mitochondria, corresponding to a red emission profile, while for stressed mitochondria the membrane potential reverses with JC-1 preferentially accumulating in the cytosol as monomers with a green emission profile. For “no” and “low” photoactivation, the red and green intensity levels remained stable, indicating a minimal change in the membrane potential of the mitochondria. For “medium” and “high” photoactivation, the red fluorescence decreased with, and without, the presence of the photosensitizer. This indicated that the activation laser (405 nm) elicits phototoxic effects upon the mitochondria (Mubaid & Brown, 2017) and thus prevented the use of the standard JC-1 metric, the ratio between red and green channels. However, at these same photoactivation levels, the green emission remained stable in the absence of the photosensitizer, while increasing in the presence of the photosensitizer. Therefore, we can infer depolarization occurred at these high-photoactivation levels.

The Bullseye Analysis was applied to the JC-1 data in the medium and high photoactivation scenarios in a similar manner as the CellROX data shown previously. However, for the

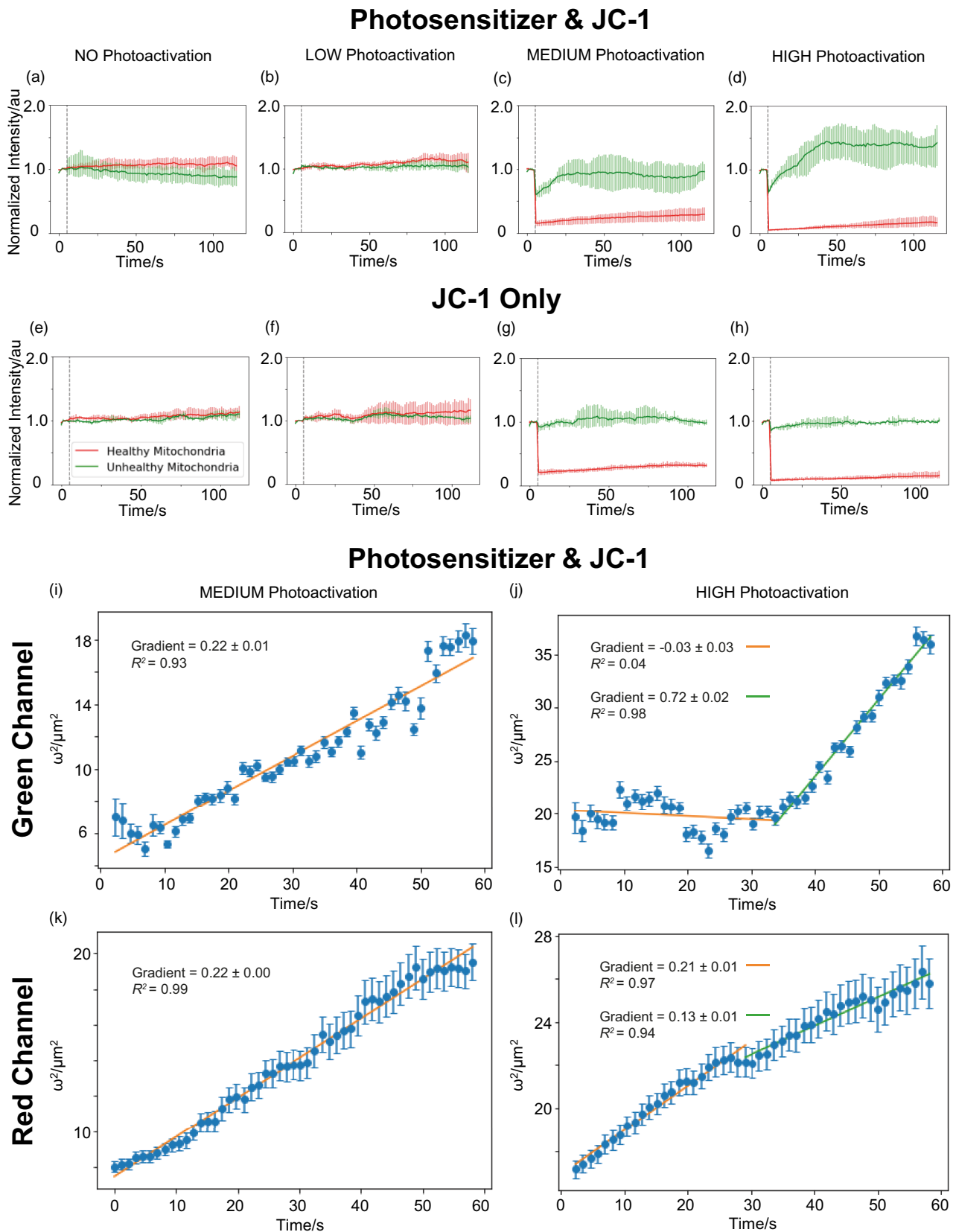


Fig. 6. Bullseye Analysis of JC-1: a fluorescent read-out of membrane polarization. Plots of JC-1 normalized fluorescence in HaCaT cells as a function of time post-photoactivation (**a–d**) photosensitizer and JC-1 and (**e–h**) JC-1 only. Red fluorescence corresponds to aggregates within healthy mitochondria and green fluorescence to monomers outside of mitochondria. Error bars are the range ($n=3$). (**i–l**) Gaussian width of the diffusion curves plotted against time for the green and red channels for photosensitizer and JC-1 in the medium and high photoactivation scenario, respectively. The gradient is calculated and plotted using linear regression and the associated standard error. In graphs (**j**) and (**l**), gradients have been calculated for the two visibly differing time windows.

red channel, the $A(t)$ term was negative due to the photo-induced reduction in fluorescence. Due to the reduction in green fluorescence immediately post-photoactivation (Supplementary Figs. S4a, S4b), all the subsequent data post-photoactivation was normalized to this baseline before fitting the data to Equation (4). This facilitated a true diffusion profile to be calculated following photoactivation and prevented any potential anomalies in the data as the green fluorescence approached and surpassed the initial pre-photoactivation fluorescence. The diffusion coefficients calculated are consistent at approximately $0.11 \mu\text{m}^2/\text{s}$ for both the green and red channels, across both medium and high photoactivation and despite the presence or absence of the photosensitizer in the case of the red channel. For high photoactivation, two trends are visible. First, no clear trend in diffusion for approximately 35 s post-photoactivation, which corresponds to continuous increase in green fluorescence within the photoactivated region. After this time, the fluorescence plateaus and diffusion takes over with a coefficient of $0.36 \pm 0.01 \mu\text{m}^2/\text{s}$.

Discussion

In this work, we propose and implement a novel technique to detect and quantify localized, subcellular ROS production (Figs. 1–3). A source of localized ROS production, via precise photoactivation of a photosensitizer, was detected by a fluorescent ROS-reporter. By varying the light dose, and thus extent of ROS production, a dose-response relationship was established between light dose, ROS production and the impact upon mitochondria. Bullseye Analysis facilitated visualization of the diffusion front between the area of localized ROS production and the immediate surrounding area and, further, how this develops with time. By equation-fitting the data to Fick's law (Tyrrell, 1964), this is a powerful tool for analyzing spatial-temporal ROS production, as well as the kinetics for more traditional FRAP experimentation. Moreover, alternative co-labels and ROS reporters could be incorporated to examine localized ROS generation and stress, all within a subcellular region.

We used the photosensitizer LightOx58 and the ROS reporter CellROX to exemplify the technique and were able to establish that localized ROS production could be measured (Fig. 2). The Bullseye Analysis (Fig. 3) went to step a further to facilitate visualization of the diffusion front and calculate the diffusion coefficient of CellROX post-photoactivation. Integrating under the Bullseye curves, the total CellROX fluorescence within, and immediately surrounding the area of photoactivation, slightly increases with time compared with the rest of the fluorescent regions. Therefore, stress and ROS production, or oxidation of CellROX within these localized regions, is potentially continuing well after photoactivation. We believe that this strongly indicates that the measured diffusion coefficient may not entirely be from diffusion alone.

As a consequence of the initial CellROX data, and in particular from finding unexpected results obtained at high photoactivation levels, we investigated the impact upon mitochondria by using the same technique with MitoTracker and JC-1 in the place of CellROX. Using MitoTracker in tandem with localized photosensitizer photoactivation (Fig. 5) was similar in methodology to Hung et al. (2018). A two-dye system was reported to examine mitochondrial morphology via GFP-mito transfected cells following localized irradiation of mitochondria-targeted photosensitizer KillerRed-dMito in

a process coined as simultaneous photoactivation and fluorescence recovery after photobleaching (SPA-FRAP; Hung et al., 2018). The cellular and mitochondrial morphology were visibly different for cells treated with the photosensitizer. Despite the photosensitizer inherently having minimal dark toxicity, the cell is slightly perturbed from its native phenotype. The photosensitizer could be acting as an “uncoupler” within the mitochondria in a similar manner to free fatty acids (FFAs; Garlid et al., 1996; Demine et al., 2019).

To examine the potential depolarization of the mitochondria in a quantitative manner, JC-1 dye was used. In the high photoactivation scenario, the green channel of JC-1 (Fig. 6) has two distinct diffusion gradients. Post-photoactivation the green fluorescence increases with time whilst no significant diffusion occurs. During this period, the mitochondria are likely to be depolarizing resulting in the efflux and conversion of JC-1 to the green fluorescing state. After approximately 30–35 s, the increase in fluorescence stops and diffusion takes over. As green fluorescing JC-1 are monomers opposed to aggregates, the higher diffusion coefficient of $0.36 \pm 0.01 \mu\text{m}^2/\text{s}$ is unsurprising compared with the red fluorescing JC-1. Interestingly, a change in diffusion was also noticed in the corresponding red channel at a similar time point. The initial diffusion coefficient, $0.11 \pm 0.01 \mu\text{m}^2/\text{s}$, agreed with the other calculated red channel coefficients before, reducing to $0.7 \pm 0.01 \mu\text{m}^2/\text{s}$. The difference in diffusion coefficient here is likely attributable to the change in micro-environment following photoactivation. Cytoplasmic viscosity has been reported to increase in response to elevated ROS levels (Wang et al., 2016; Li et al., 2019) while similar viscosity increases have been found following photosensitizer photoactivation (Kuimova et al., 2009; Aubertin et al., 2013).

Through the use of small molecules and no genetic modification, we have been able to develop a technique suitable for the study of localized ROS generation at the subcellular scale. We believe through the use of exogenous fluorophores and our new analysis protocol, our method will provide researchers with a new approach to help understand localized ROS production, an area of growing importance both to understand basic biological process and for the development of new photodynamic therapeutics.

Conclusion

We have provided and exemplified a technique that is suitable for examining subcellular effects of localized perturbations upon cells in a spatial and time-dependent manner. By altering experimental factors such as the compound or light dose, dose-response data can be collected, potentially facilitating drug optimization in cellular environments which could be extended to tumor work. While we have examined ROS production, quantification, diffusion coefficients, and subsequent mitochondrial impact in this work, many other photoactivatable compounds, drugs, or co-stains, could be substituted or alternative analyses used to build up a broader understanding of the impact upon the cell. This technique provides a novel method for examining localized ROS production and the impact upon the cell at the subcellular level.

Supplementary material

To view [supplementary material](https://doi.org/10.1093/micmic/ozac040) for this article, please visit <https://doi.org/10.1093/micmic/ozac040>.

Acknowledgments

The authors thank Valerie Affleck and Daniel Callaghan for help in tissue culture, as well as Penny Lawton and Cole Sims for their scientific input.

Author contributions statement

J.G.H., C.A.A., and J.M.G. wrote the main manuscript text and J.G.H. prepared the figures. J.G.H., J.G.M., and C.A.A. designed the experiments and J.G.H. carried out the experiments. All authors reviewed the manuscript.

Financial support

This work was funded in part by EPSRC award EP/R511523/1.

Conflict of interest

A.W. and C.A.A. own shares of LightOx Limited, the company licensed to pursue commercial applications of the novel compounds described in this manuscript. J.G.H., D.R.C., and J.M.G. declare no competing interests.

References

- Aubertin K, Bonneau S, Silva AKA, Bacri J-C, Gallet F & Wilhelm C (2013). Impact of photosensitizers activation on intracellular trafficking and viscosity. *PLoS ONE* 8(12), e84850.
- Baptista MS, Cadet J, Di Mascio P, Ghogare AA, Greer A, Hamblin MR, Lorente C, Nunez SC, Ribeiro MS, Thomas AH, Vignoni M & Yoshimura TM (2017). Type I and type II photosensitized oxidation reactions: Guidelines and mechanistic pathways. *Photochem Photobiol* 93(4), 912–919.
- Chisholm DR, Hughes JG, Blacker TS, Humann R, Adams C, Callaghan D, Pujol A, Lembicz NK, Bain AJ, Girkin JM, Ambler CA & Whiting A (2020). Cellular localisation of structurally diverse diphenylacetylene fluorophores. *Org Biomol Chem* 18(45), 9231–9245.
- Chisholm DR, Lamb R, Pallett T, Affleck V, Holden C, Marrison J, O'Toole P, Ashton PD, Newling K, Steffen A, Nelson AK, Mahler C, Valentine R, Blacker TS, Bain AJ, Girkin J, Marder TB, Whiting A, Ambler CA (2019). Photoactivated cell-killing involving a low molecular weight, donor-acceptor diphenylacetylene. *Chem Sci* 10(17), 4673–4683.
- Cross CE, Halliwell B, Borish ET, Pryor WA, Ames BN, Saul RL, McCORD JOEM & Harman D (1987). Oxygen radicals and human disease. *Ann Internal Med* 107(4), 526–545.
- de Albuquerque IO, Nunes J, Longo JPF, Muehlmann LA & Azevedo RB (2019). Photodynamic therapy in superficial basal cell carcinoma treatment. *Photodiagn Photodyn Ther* 27, 428–432.
- Demine S, Renard P & Arnould T (2019). Mitochondrial uncoupling: A key controller of biological processes in physiology and diseases. *Cells* 8(8), 795.
- de Pablo JG, Chisholm DR, Ambler CA, Peyman SA, Whiting A & Evans SD (2020). Detection and time-tracking activation of a photosensitizer on live single colorectal cancer cells using Raman spectroscopy. *Analyst* 145(17), 5878–5888.
- de Pablo JG, Chisholm DR, Steffen A, Nelson AK, Mahler C, Marder TB, Peyman SA, Girkin JM, Ambler CA, Whiting A & Evans SD (2018). Tandem fluorescence and Raman (fluoroRaman) characterisation of a novel photosensitizer in colorectal cancer cell line SW480. *Analyst* 143(24), 6113–6120.
- Finkel T (1998). Oxygen radicals and signaling. *Curr Opin Cell Biol* 10(2), 248–253.
- Fuloria S, Subramaniyan V, Karupiah S, Kumari U, Sathasivam K, Meenakshi DU, Wu YS, Sekar M, Chitranshi N, Malviya R, Sudhakar K, Bajaj S & Fuloria NK (2021). Comprehensive review of methodology to detect reactive oxygen species (ROS) in mammalian species and establish its relationship with antioxidants and cancer. *Antioxidants* 10(1), 128.
- Garlid KD, Orosz DE, Modrianský M, Vassanelli S & Jezek P (1996). On the mechanism of fatty acid-induced proton transport by mitochondrial uncoupling protein. *J Biol Chem* 271(5), 2615–2620.
- Girkin J (2019). *A Practical Guide to Optical Microscopy*. London: CRC Press.
- Holmström KM & Finkel T (2014). Cellular mechanisms and physiological consequences of redox-dependent signalling. *Nat Rev Mol Cell Biol* 15(6), 411–421.
- Hung CH-L, Cheng SS-Y, Cheung Y-T, Wuwongse S, Zhang NQ, Ho Y-S, Lee SM-Y & Chang RC-C (2018). A reciprocal relationship between reactive oxygen species and mitochondrial dynamics in neurodegeneration. *Redox Biol* 14, 7–19.
- Kang M, Day CA, Kenworthy AK & DiBenedetto E (2012). Simplified equation to extract diffusion coefficients from confocal FRAP data. *Traffic* 13(12), 1589–1600.
- Kuimova MK, Botchway SW, Parker AW, Balaz M, Collins HA, Anderson HL, Suhling K & Ogilby PR (2009). Imaging intracellular viscosity of a single cell during photoinduced cell death. *Nat Chem* 1(1), 69–73.
- Li H, Shi W, Li X, Hu Y, Fang Y & Ma H (2019). Ferroptosis accompanied by $\cdot\text{OH}$ generation and cytoplasmic viscosity increase revealed via dual-functional fluorescence probe. *J Am Chem Soc* 141(45), 18301–18307.
- Mubaid F & Brown CM (2017). Less is more: Longer exposure times with low light intensity is less photo-toxic. *Microsc Today* 25(6), 26–35.
- Murfin LC, Weber M, Park SJ, Kim WT, Lopez-Alled CM, McMullin CL, Pradaux-Caggiano F, Lyall CL, Kociok-Köhn G & Wenk J (2019). Azulene-derived fluorescent probe for bioimaging: Detection of reactive oxygen and nitrogen species by two-photon microscopy. *J Am Chem Soc* 141(49), 19389–19396.
- Nespolo M (2017). Free radicals in biology and medicine. By Barry Halliwell and John MC Gutteridge. Oxford University Press, 2015. Pp. xxxviii+ 905. Price GBP 70.00 (paperback, ISBN 9780198717485), GBP 125.00 (hardback, ISBN 9780198717478). *Acta Crystallogr Sect D Struct Biol* 73(4), 384–385.
- Ott M, Gogvadze V, Orrenius S & Zhivotovsky B (2007). Mitochondria, oxidative stress and cell death. *Apoptosis* 12(5), 913–922.
- Poot M, Zhang Y-Z, Krämer JA, Sam Wells K, Jones LJ, Hanzel DK, Lugade AG, Singer VL & Haugland RP (1996). Analysis of mitochondrial morphology and function with novel fixable fluorescent stains. *J Histochem Cytochem* 44(12), 1363–1372.
- Schindelin J, Arganda-Carreras I, Frise E, Kaynig V, Longair M, Pietzsch T, Preibisch S, Rueden C, Saalfeld S, Schmid B, Tinevez J-Y, White DJ, Hartenstein V, Eliceiri K, Tomancak P & Cardona A (2012). Fiji: An open-source platform for biological-image analysis. *Nat Methods* 9(7), 676–682.
- Schneider CA, Rasband WS & Eliceiri KW (2012). NIH Image to ImageJ: 25 years of image analysis. *Nat Methods* 9(7), 671–675.
- Seiffert S & Oppermann W (2005). Systematic evaluation of FRAP experiments performed in a confocal laser scanning microscope. *J Microsc* 220(1), 20–30.
- Sies H (2019). *Oxidative Stress: Eustress and Distress*. London: Academic Press.
- Tyrrell HJV (1964). The origin and present status of Fick's diffusion law. *J Chem Educ* 41(7), 397.
- Wang H, Zhang R, Bridle KR, Jayachandran A, Thomas JA, Zhang W, Yuan J, Xu ZP, Crawford DH & Liang X (2017). Two-photon dual imaging platform for in vivo monitoring cellular oxidative stress in liver injury. *Sci Rep* 7(1), 1–11.

- Wang X, Fang H, Huang Z, Shang W, Hou T, Cheng A & Cheng H (2013). Imaging ROS signaling in cells and animals. *J Mol Med* **91**(8), 917–927.
- Wang X, Song F & Peng X (2016). A versatile fluorescent probe for imaging viscosity and hypochlorite in living cells. *Dyes Pigments* **125**, 89–94.
- Zhang J, Jiang C, Longo JPF, Azevedo RB, Zhang H & Muehlmann LA (2018a). An updated overview on the development of new photosensitizers for anticancer photodynamic therapy. *Acta Pharm Sin B* **8**(2), 137–146.
- Zhang Y, Dai M & Yuan Z (2018b). Methods for the detection of reactive oxygen species. *Anal Methods* **10**(38), 4625–4638.